



HAL
open science

Hybrid organic-inorganic nanotubes effectively adsorb some organic pollutants in aqueous phase

Roberto Nasi, Filomena Sannino, Pierre Picot, Antoine Thill, Olimpia Oliviero, Serena Esposito, Marco Armandi, Barbara Bonelli

► To cite this version:

Roberto Nasi, Filomena Sannino, Pierre Picot, Antoine Thill, Olimpia Oliviero, et al.. Hybrid organic-inorganic nanotubes effectively adsorb some organic pollutants in aqueous phase. *Applied Clay Science*, 2020, 186, pp.105449. 10.1016/j.clay.2020.105449 . cea-02458782

HAL Id: cea-02458782

<https://cea.hal.science/cea-02458782>

Submitted on 21 Jul 2022

HAL is a multi-disciplinary open access archive for the deposit and dissemination of scientific research documents, whether they are published or not. The documents may come from teaching and research institutions in France or abroad, or from public or private research centers.

L'archive ouverte pluridisciplinaire **HAL**, est destinée au dépôt et à la diffusion de documents scientifiques de niveau recherche, publiés ou non, émanant des établissements d'enseignement et de recherche français ou étrangers, des laboratoires publics ou privés.



Distributed under a Creative Commons Attribution - NonCommercial 4.0 International License

1 **Hybrid organic-inorganic nanotubes effectively adsorb some organic pollutants in aqueous**
2 **phase**

3
4 Roberto Nasi,^{1,§} Filomena Sannino,² Pierre Picot,^{3,§} Antoine Thill,³ Olimpia Oliviero,⁴ Serena
5 Esposito,¹ Marco Armandi,¹ Barbara Bonelli^{1,*}

6
7 ¹*LIONS, NIMBE, CEA, CNRS, Université Paris-Saclay, CEA-Saclay, Gif-sur-Yvette, 91191, France*

8 ²*Department of Agricultural Sciences– Università degli Studi di Napoli Federico II, 80055 Portici-*
9 *Napoli, Italy*

10 ³*Department of Applied Science and Technology & INSTM Unit of Torino Politecnico - Politecnico*
11 *di Torino, 10129 Torino, Italy*

12 ⁴*Department of Neuroscience and Reproductive and Odontostomatologic Sciences, Università degli*
13 *Studi di Napoli Federico II, 80055 Portici- Napoli, Italy*

14
15 **Keywords:** imogolite; SAXS; hybrid nanotubes; MCPA; herbicides; dichloromethane

16 Corresponding author: *barbara.bonelli@polito.it

17 [§] Both authors equally contributed to the paper.

18

19

20

21

22

23

24

25

26

27 **Abstract**

28 Methylimogolite nanotubes (Me-IMO NTs, chemical composition $(\text{OH})_3\text{Al}_2\text{O}_3\text{SiCH}_3$) are
29 characterized by having an inner hydrophobic (fully-methylated) surface. Conversely, the outer
30 surface is hydrophilic and positively charged below the point of zero charge (at $\text{pH} = 8.6$), due to
31 the $\text{Al}(\text{OH})\text{Al} + \text{H}^+ = \text{Al}(\text{OH})_2^+\text{Al}$ equilibrium occurring at the outer surface of the NTs when they
32 are dispersed in water.

33 In this work, adsorption of MCPA (2-methyl-4-chlorophenoxyacetic acid) and of
34 dichloromethane (DCM) on Me-IMO NTs was studied by means of both adsorption/desorption
35 measurements in batch conditions (at room temperature and at different pH value) and Small Angle
36 X-rays Scattering (SAXS).

37 MCPA, which partially dissociates in water ($\text{pK}_a = 2.90$), is mainly adsorbed at the outer
38 surface of the NTs, although measurements in batch conditions show that other types of interaction
39 occur (i.e. H-bond) at higher MCPA concentration. SAXS measurements confirm that MCPA has
40 not entered the NTs inner pores.

41 Interaction of the NTs with DCM, instead, is more complex: SAXS measurements show that
42 DCM molecules interact with the NTs inner surface, whereas batch experiments indicate that
43 additional interactions take place with the outer surface of the NTs.

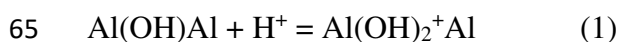
44
45
46
47
48
49
50
51
52

53 **Introduction**

54 Hybrid organic-inorganic nanotubes (NTs) with chemical formula $(\text{OH})_3\text{Al}_2\text{O}_3\text{SiCH}_3$ (Me-
55 IMO) can be synthesized in water by a template-free sol-gel procedure, starting from commercial
56 precursors, i.e. an Al salt (or alkoxide) and triethoxymethylsilane (TEMS) (Bottero et al., 2011).
57 Dual functionalization of the inner surface is also possible to a certain extent (Picot et al., 2019) and
58 Ge-analogues can be obtained, as well (Amara et al., 2015).

59 Me-IMO NTs have unique properties: they are mainly mesoporous with remarkably high
60 accessible specific surface area (about $650 \text{ m}^2 \text{ g}^{-1}$) and are thermally stable up to $300 \text{ }^\circ\text{C}$
61 (Mackenzie, 1989; Bottero et al., 2011). When dispersed in water, the NTs are positively charged at
62 pH values below 9 (Bahadori et al., 2018). Such positive charge stems, in part, from the acid-base
63 properties of external -OH groups (Gustafsson, 2001) as in eq. (1):

64



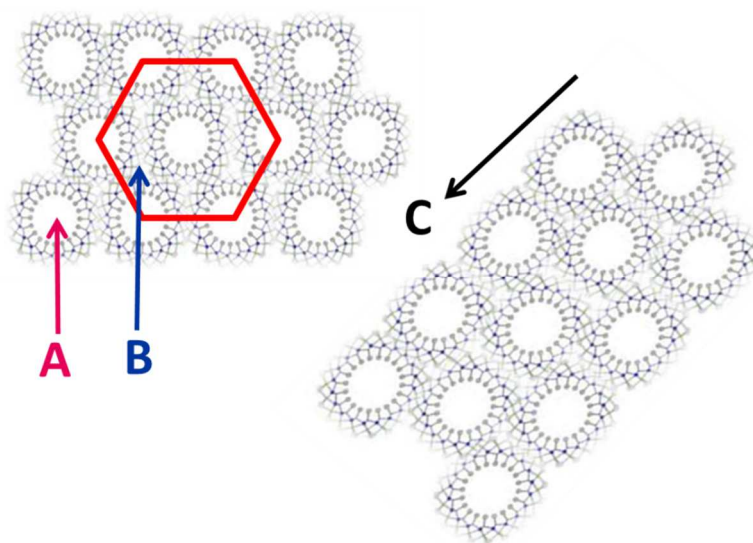
66

67 and, in part, from some curvature effects (Poli et al., 2015).

68 Proper (inorganic) imogolite (IMO) NTs (Cradwick et al., 1972), which can be obtained by
69 sol-gel methods as well (Du et al., 2017), have different structure (Thill et al., 2017) and
70 applications, depending on whether they occur as a powder or in aqueous suspension of freshly
71 synthesized NTs. Aqueous dispersions of pristine IMO NTs, which have never been dried, do not
72 show any bundles, since the NTs repel each other, due to their positive surface charge. The NTs
73 may form bundles upon addition of salt or upon increase of pH. In such a case, bundles formation is
74 irreversible to a large extent (Karube, 1998).

75 Surprisingly, even in freshly synthesized dispersions, Me-IMO NTs are always observed to
76 form bundles (Scheme 1), where three types of pores A, B and C can be identified (Ackerman et al.,
77 1993). Noticeably, in Me-IMO the A pores have an average diameter of 2.0 nm and are extremely
78 hydrophobic, whereas in IMO they have an average diameter of 1.0 nm and are extremely

79 hydrophilic (Bonelli et al., 2009; Zanzottera et al., 2012b); the B pores are 0.45 nm wide in Me-
80 IMO, allowing adsorption of small probes in gas/solid systems (Zanzottera et al., 2012a; Bonelli et
81 al., 2013a), being instead smaller in IMO (*ca.* 0.30 nm) and, thus, less accessible to gas probes
82 (Ackerman et al., 1993). Finally, the C pores (Scheme 1) are larger slit-mesopores, accessible to
83 large molecules (Garrone and Bonelli, 2016; Shafia et al., 2016a) and characterized by amphoteric
84 properties (Bonelli et al., 2009, 2013b) in both Me-IMO and IMO.



85

86

Scheme 1.

87 Three types of pores occurring in Me-IMO NTs in the powder form.

88

89 Although also gels may be obtained, usually powders of Me-IMO NTs are obtained (Bottero
90 et al., 2011). In water, the positively charged outer surface (eq. 1) favours both NTs re-dispersion,
91 and interaction with negatively charged species (Bonelli, 2016) and/or polar molecules (Boyer et
92 al., 2014). Nonetheless, some of us showed that in oil-in-water emulsion, Me-IMO NTs adsorb at
93 the oil/water interface, stabilizing the emulsion by inducing slow oil-triggered modifications of the
94 viscosity of the continuous phase and, possibly, favouring transport of small molecules within the NTs
95 (Picot et al., 2016).

96 With Me-IMO NTs, the simultaneous occurrence of an inner hydrophobic surface and an
97 outer hydrophilic (and positively charged surface) may be of interest in applications implying

98 selective adsorption, like gas membranes, adsorption of complex mixtures and removal of water
 99 pollutants, as well. Indeed, IMO has been proposed as an optimal adsorbent of anions and, in
 100 particular, for phosphate fixation at the outer surface of the NTs (Mizota, 1977; Parfitt, 2009; Rojas-
 101 Mancilla et al., 2019).

102 There is currently a great interest into the development of new nanomaterials able to
 103 efficiently remove from water several organic pollutants, besides inorganic ones, like
 104 agrochemicals, dyes, halogenated compounds, pharmaceutical and personal care products, etc.
 105 (Freyria et al., 2018). Some of us studied the adsorption and degradation of the azo-dye Acid
 106 Orange 7 (AO7, C₁₆H₁₁N₂SO₄Na) in the presence of aqueous suspensions of IMO, Me-IMO or
 107 Fe³⁺-doped NTs (Shafia et al., 2016a; Bahadori et al., 2018). Some interesting insights were
 108 obtained, like the preferential interaction of AO7 moieties (negatively charged in water) with the
 109 outer surface of NTs, although some of the inner Si-OH groups of IMO NTs (likely those at the
 110 mouth of A pores) were able to interact with the pollutant by H-bonding. In the presence of
 111 Fe³⁺ species, instead, a ligand displacement phenomenon was observed, where Fe³⁺ ions were able
 112 to coordinate the dye through its N atoms. (Shafia et al., 2016a). This work focuses, instead, on the
 113 interaction of Me-IMO NTs with two organic molecules (Table 1) in water suspension, namely 4-
 114 chloro-2-methylphenoxyacetic acid (MCPA) and dichloromethane (DCM).

115

116 **Table 1**

117 Some properties of MCPA and DCM.

Pollutant	Molecule dimension(s) (nm)	Dipole Moment (D)	pKa	Solubility in water (g/L)	Bulk Electron density (e⁻/Å³)
MCPA	~ 0.8 x 0.7		2.90	0.825 at 23 °C ^b	0.480
DCM	0.33 ^a	1.470	-	17.5 at 25 °C	0.396

118 ^aKinetic diameter

119 ^b(Gimeno et al., 2003)

120

121 MCPA is a phenoxy herbicide extensively used in agriculture to control annual and
 122 perennial weeds in cereals, grasslands, trees and turf: being highly soluble in water and very mobile,

123 it can leach from soil and can be found in groundwater wells, thus posing serious environmental
124 problems. For this reason, the U.S. Environmental Protection Agency (EPA) classifies MCPA as a
125 potential groundwater contaminant (Addoriso et al., 2010).

126 DCM is a chlorinated volatile organic compound (VOC), which is soluble in water due to its
127 dipole moment ($\mu_{\text{DCM}} = 1.470 \text{ D}$): it is mainly used as solvent and reagent, being also employed in
128 the manufacture of aerosols, adhesives, and for dry cleaning (Huang et al., 2014). In addition to its
129 high toxicity and carcinogenic character, DCM contributes to global warming, depletion of the
130 ozone layer, and photochemical smog: the U.S. EPA has included it among the 17 highly dangerous
131 chemicals that should be targeted for emissions reduction.

132 In this work, a sample of Me-IMO NTs was characterized by powder X-ray Diffraction
133 (XRD), N_2 isotherms at $-196 \text{ }^\circ\text{C}$, ζ -potential measurements and SAXS and was tested as adsorbent
134 of either MCPA or DCM by means of adsorption/desorption experiments in batch conditions and by
135 SAXS.

136

137 **2. Materials and Methods**

138 *2.1 Me-IMO synthesis*

139 A sample of Me-IMO was synthesized according to a procedure reported elsewhere (Bottero
140 et al., 2011). In acidic medium due to HClO_4 , Al-*sec*-butoxide (ASB) and triethoxymethylsilane
141 (TEMS) were used as the Al and Si source, respectively, with molar ratio Al : Si = 2 : 1.15. The
142 slight excess of TEMS was used to prevent formation of by-products (i.e. Al hydroxide) due to fast
143 hydrolysis of ASB, which is a crucial issue in the synthesis. For the same reason, the sample was
144 synthesised in a dry room (i.e. a moisture-free environment) (Shafia et al., 2016b).

145

146 *2.2. Me-IMO characterization*

147 X-ray powder diffraction (XRD) were measured in the $2.5\text{--}20^\circ$ 2θ range on an 'Xpert
148 Diffractometer (Cu $\text{K}\alpha$ radiation; $\lambda=1.5414 \text{ \AA}$, step width = $0.02 \text{ } 2\theta$).

149 The values of BET SSA (Brunauer Emmett Teller Specific Surface Area), total pore volume
150 and *t-plot* microporous volume reported in Table 2 were calculated from the N₂
151 adsorption/desorption isotherm measured at -196 °C on the powder outgassed at 275 °C in order to
152 remove residual water and atmospheric contaminants. The Non Local-Density Function Theory
153 Pore Size Distribution (NL-DFT PSD) and the corresponding cumulative pore volume curve were
154 obtained by applying a N₂-silica kernel (for cylindrical pores) to the isotherm adsorption branch.

155 The Al/Si ratio was measured by means of Energy Dispersive X-ray analysis (EDX, AZTec,
156 Oxford Instruments) on three different spots (ca. 0.1 mm² area each): the so-obtained average value
157 Al/Si = 0.49 was in fair agreement with the theoretical one Al/Si = 0.50.

158 Electrophoretic mobility as a function of pH was measured at 25°C by means of light
159 scattering technique on a Zetasizer Nano-ZS instrument (Malvern Instruments, Worcestershire,
160 UK). The corresponding ζ -potential curve was calculated according to the Henry's equation $UE =$
161 $2\varepsilon\zeta f(Ka)/3\eta$, where UE is the electrophoretic mobility, ε is the dielectric constant, ζ is the zeta
162 potential, $f(Ka)$ is the Henry's function, and η is the viscosity. The adopted value of $f(Ka)$ was 1.5,
163 in agreement with the Smoluchowski approximation, usually applied to aqueous solutions of
164 moderate electrolyte concentration, as in the present case. Water suspensions were obtained after 2
165 min sonication with an ultrasonic probe (100 W, 20 kHz, Sonoplus; Bandelin, Berlin, Germany); the
166 pH of the suspension was then adjusted by adding either 0.10 M HCl or 0.10 M NaOH.

167 SAXS (Small Angle X-ray Scattering) data were acquired on a Xeuss 2.0 HR SAXS/WAXS
168 instrument (Xenocs) equipped with a microfocus Copper sealed tube (30 W/30 μ m) ; single
169 reflection multilayer optic with 2D collimation for Cu K α ($\lambda=1.5414$ Å) and 2 motorized scatter-
170 less slits 2.0 with variable aperture enable the definition of the beam energy (Cu K α with spectral
171 purity > 97 %) and size while minimizing the scattering background. The divergence of the beam is
172 < 0.4 mrad in both planes perpendicular to beam axis. The sample were measure in the high
173 resolution beam configuration with a max flux at the sample position of 1×10^8 (ph/s).

174 Me-IMO NTs were studied both as powder and in water suspension: in the former case, the
175 powder was fixed between two Kapton films and placed in aluminium frame (Fig. 6), whilst glass
176 capillaries containing dispersion and contaminants were vacuum tight sealed and placed in a
177 different aluminium sample holder that can accommodate up to 20 capillaries.

178 MCPA adsorption on MeIMO has been evaluated by SAXS, as follows: a stock dispersion
179 of 5g/L of MeIMO in 100 μ M of herbicide water (MilliQ) solution was prepared (natural pH 4.45).
180 From the stock MeIMO dispersion three samples were also prepared at different pH (3, 4.45, 9.65,
181 10.46) by means of HCl or NH₃ addition.

182 DCM adsorption on Me-IMO has been evaluated by SAXS at natural pH.

183

184 *2.3 Adsorption/desorption experiment in batch-conditions*

185 4-chloro-2-methylphenoxyacetic acid (MCPA) and Dichloromethane (DCM) were
186 purchased from Sigma-Aldrich Chemical Co. (Poole, Dorset, U.K.; 99.0% purity). HPLC grade
187 solvents (Carlo Erba, Milan, Italy) were used without further purification. All the other chemicals
188 were from Sigma-Aldrich, unless otherwise specified.

189 For MCPA experiments, a stock solution of the herbicide was prepared by dissolving 200
190 mg MCPA in 1000 mL of ultrapure water (final concentration 1000 μ mol L⁻¹) and, then, kept
191 refrigerated.

192 For DCM experiments, a stock solution of the organic pollutant was prepared by diluting
193 DCM with ultrapure water (final concentration 0.15 mol L⁻¹).

194

195 *2.3.1 Analytical determination of the organic contaminants*

196 The concentration of MCPA was measured on an Agilent 1200 Series HPLC apparatus
197 (Wilmington, DE), equipped with a DAD array and a ChemStation Agilent Software. A Macharey-
198 Nagel Nucleosil 100-5 C18 column (stainless steel 250 4 mm) was used.

199 For MCPA determination, the mobile phase, comprising a binary system of 50:50
200 acetonitrile: phosphate buffer (0.1%, pH 2.5), was pumped at 1 mL min⁻¹ flow in isocratic mode.
201 The UV detector was set at 225 nm. The quantitative determination of MCPA was performed by
202 elaborating its corresponding calibration curve in the 0.25 - 1000 µmol L⁻¹ range.

203 The concentration of DCM was determined by Gas Chromatography-Mass Spectrometry
204 (GC-MS). The samples were analysed on a Perkin-Elmer AutoSystemTMXL GC, equipped with a
205 Programmed-Temperature Split/Splitless injector with programmable pneumatic control kept at a
206 constant temperature of 250 °C; a Restek Rtx-5MS capillary column (5% diphenyl-95%
207 dimethylpolysiloxane, 30 m x 0.25 mm, 0.25 µm) and a Perkin-Elmer Turbo Mass Goldmass-
208 spectrometer. The oven temperature was programmed to run at 60 °C for 5 min and then to increase
209 by 15 °C min⁻¹ to a final temperature of 280 °C. A NIST mass spectral library version 1.7 was used
210 for peak identification. The quantitative determination of DCM was performed elaborating its
211 corresponding calibration curve in the 0.0125 and 0.15 mol L⁻¹ range.

212 213 *2.3.2 Study of the effect of pH, time and concentration of MCPA*

214 To evaluate the effect of pH, MCPA sorption experiments were carried out at solid/liquid
215 ratio of 0.5 g L⁻¹ obtained by adding 5 mg of NTs to a final volume of 10 mL, using a fixed
216 pesticide concentration of 10 µmol L⁻¹, obtained by diluting 1000 µmol L⁻¹ stock solution, varying
217 the pH from 3.0 to 9.5 and for an incubation time of 24 h. The pH was controlled by addition of
218 0.01 mmol L⁻¹ HCl or NaOH to the solution. After incubation in a rotatory shaker at 20 °C, the
219 samples were centrifuged at 7000 rpm for 20 min. The amount of adsorbed MCPA was calculated
220 as the difference between the MCPA quantity initially added and that present in the liquid at
221 equilibrium. Blanks of MCPA in ultrapure water were analyzed in order to check for pesticide
222 stability and/or sorption on the vials.

223 To evaluate the effect of time on MCPA adsorption, experiments were performed at
224 solid/liquid ratio of 0.5 g L⁻¹ using 7.0 µmol L⁻¹ of MCPA at pH 3.5. The suspensions were stirred

225 for 2.0, 5.0, 10, 20, 40, 60, 90, 120, 300, 1080, 1440, 1680 and 2880 min. Different volumes of a
226 stock solution of herbicide ($1000 \mu\text{mol L}^{-1}$) were added to the NTs containing liquid to have initial
227 MCPA concentration in the $0.05 - 260 \mu\text{mol L}^{-1}$ range. The pH was kept constant at 3.5 by addition
228 of 0.10 or 0.01 mol L^{-1} HCl or NaOH. The samples were incubated for 1440 min and, then, after
229 centrifugation, the supernatants were analyzed as described above.

230 During desorption experiments, immediately after adsorption of 255 and $170 \mu\text{mol L}^{-1}$ initial
231 MCPA concentration, the samples were put in contact with different volumes of ultrapure water, so
232 to determine the amount of released herbicide. In particular, 10 mL of supernatant was removed and
233 replaced with 10 mL of ultrapure water. After shaking at $25 \text{ }^\circ\text{C}$ for 24 h , the suspensions were
234 centrifuged and the concentration of released herbicide in the supernatant was determined. The
235 same procedure was repeated by replacing 3.0 , 4.0 , and 6.0 mL of supernatant with the same
236 volume of ultrapure water.

237 238 *2.3.3 Study of the effect of pH, time and concentration of DCM*

239 In order to study the effect of pH, sorption experiments were made at a solid/liquid ratio of
240 0.5 g L^{-1} obtained by adding 5 mg solid to a final volume of 10 mL , using a constant DCM
241 concentration of 0.15 mol L^{-1} , varying the pH from 3.5 to 7.0 and with an incubation time of 24 h .
242 pH was controlled by addition of 0.01 mmol L^{-1} HCl or NaOH. After incubation in a rotatory shaker
243 at $20 \text{ }^\circ\text{C}$, the samples were centrifuged at 7000 rpm for 20 min . The amount of adsorbed DCM was
244 calculated as the difference between the initially added quantity of DCM and the quantity present at
245 equilibrium in the liquid. Blanks of DCM in ultrapure water were analysed in order to check for
246 pollutant stability and sorption on the vials.

247 In order to study the effect of time, experiments were performed at a solid/liquid ratio of 0.5
248 g L^{-1} by using 0.15 mol L^{-1} of DCM at pH 5.5 . The suspensions were stirred for 2.0 , 5.0 , 10 , 20 , 40 ,
249 60 , 90 , 120 , 300 , 1080 , 1440 , 1680 and 2880 min .

250 The adsorption isotherm was obtained as follows: different volumes of a stock solution of
251 DCM (0.15 mol L^{-1}) were added to the Me-IMO NTs containing liquid in such a way to have an
252 initial DCM concentration in the $0.0125 - 0.15 \text{ mol L}^{-1}$ range. The pH of each suspension was kept
253 constant at 5.5 by adding 0.10 or 0.01 mol L^{-1} HCl or NaOH. The samples were incubated for 300
254 min and, then, after centrifugation, the supernatants were analysed as described above.

255 During desorption experiments, the sample obtained immediately after adsorption from 0.15
256 mol L^{-1} DCM initial concentration, was put in contact with different volumes of ultrapure water at
257 standard pH value, so to determine the amount of released DCM. In particular, 10 mL of
258 supernatant was removed and replaced by 10 mL of ultrapure water. After shaking at $25 \text{ }^\circ\text{C}$ for 5 h ,
259 the suspension was centrifuged and the concentration of released DCM was determined. The same
260 procedure was made by replacing 3.0 , 4.0 , and 6 mL of supernatant with the same volume of
261 ultrapure water.

262

263 **3. Results and discussion**

264 *3.1. Relevant physico-chemical features of the Me-IMO NTs in powder and water*
265 *suspension.*

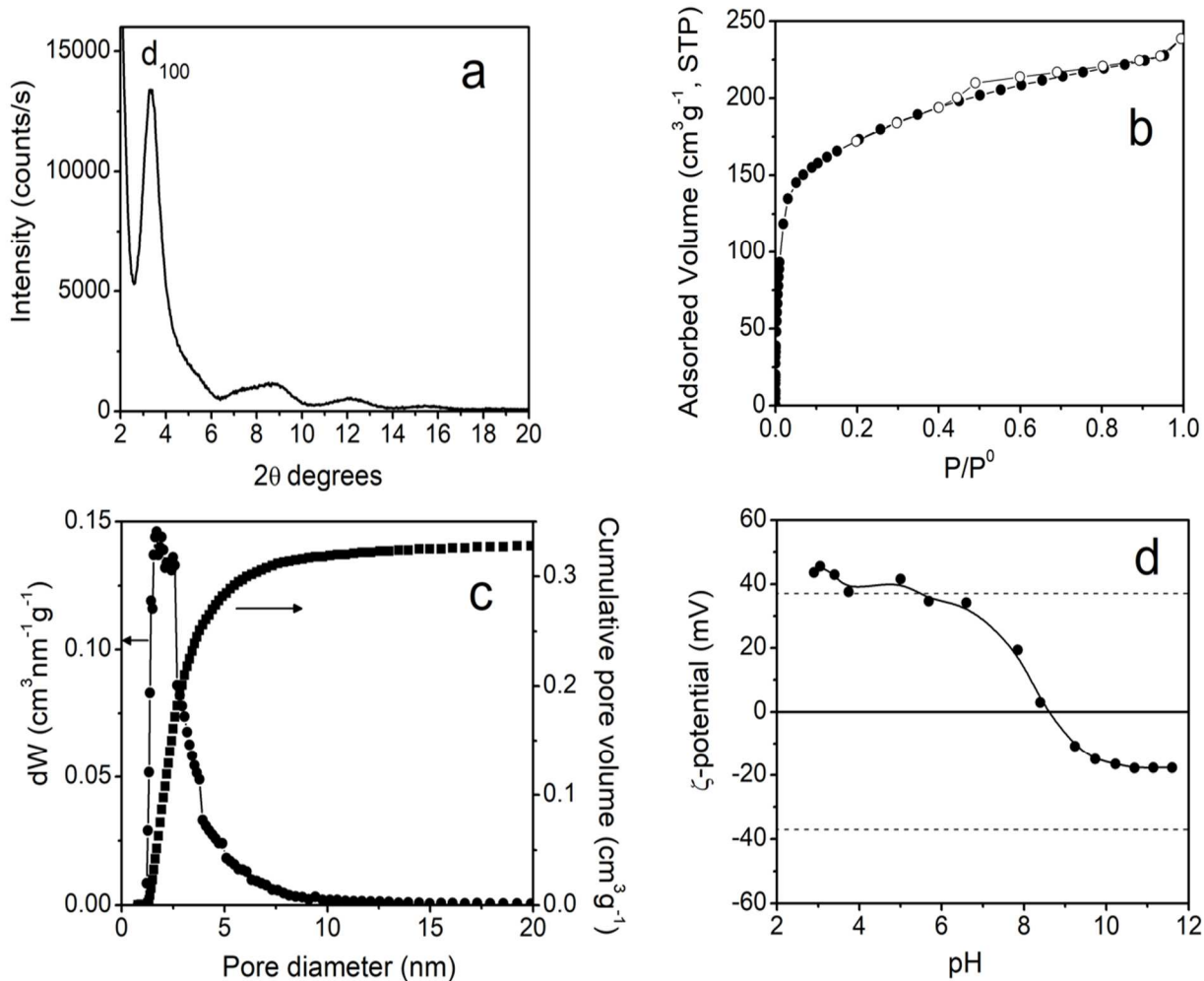
266 Figure 1 reports the powder XRD pattern (a), the N_2 adsorption/desorption isotherm at -196
267 $^\circ\text{C}$ (b), the PSD and cumulative volume (c) and the ζ -potential curve (d) of the Me-IMO NTs. In
268 Fig. 1a, the main reflection at $3.32 \text{ } 2\theta$ and the halo at $8.84 \text{ } 2\theta$ degrees are characteristic of NTs
269 organized into a pseudo-hexagonal arrangement (Bursill et al., 2000; Bottero et al., 2011). The
270 value of the cell parameter (Table 2) was $a = 3.02 \text{ nm}$, as calculated by applying the equation $a =$
271 $\frac{2}{\sqrt{3}}d_{100}$: the cell parameter is larger than that of IMO NTs (Cradwick et al., 1972), due to larger A
272 pores (*vide infra*).

273 Fig. 1b shows a type IV N_2 isotherm, with a limited (type H4) hysteresis loop. The steep
274 increase of the adsorbed volume at low P/P^0 values indicates occurrence of some micropores,

275 whereas the rounded knee below 0.1 P/P^0 is due to the presence of very narrow mesopores. The
276 corresponding values of BET SSA and pore volume (Table 2) are typical of Me-IMO NTs (Bottero
277 et al., 2011). Accordingly, the PSD curve (circles in Fig. 1c) shows the occurrence of (mainly)
278 narrow mesopores with an average diameter of *ca.* 2.0 nm (A pores). The value of micropore
279 volume that can be extrapolated from the cumulative pore volume curve (squares in Fig. 1c) is close
280 to that reported in Table 2, which is obtained by the *t*-plot method ($0.085 \text{ cm}^3 \text{ g}^{-1}$).

281 The ζ -potential curve (Fig. 1d) shows that the NTs are positively charged in a broad pH
282 range, and have a point of zero charge equal to 8.6. Nonetheless, the lines at $\zeta = \pm 37 \text{ mV}$ show
283 range of ζ potential reported in the literature for stable suspensions (Honary and Zahir, 2013),
284 indicating that above pH = 5 some NTs aggregation may occur. Such a phenomenon could affect
285 the adsorption/desorption experiments (*vide infra*).

286



287

288

289

290

291

292

293

294

295

Figure 1. Section a: low angle XRD pattern of Me-IMO powder; section b: N₂ isotherm at -196 °C (black symbols: adsorption branch; white symbols: desorption branch); section c: NL-DFT PSD (circles) and cumulative pore volume (squares) as obtained by applying a N₂ - silica kernel to the isotherm adsorption branch; section d: ζ-potential curve of Me-IMO NTs as a function of pH.

Table 2. Some textural properties of Me-IMO NTs as obtained by N₂ isotherms at -196 °C,

X-ray powder diffraction and SAXS experiments with either the dry powder or the water dispersed one.

Sample	BET SSA (m ² g ⁻¹)	Total Pore Volume (cm ³ g ⁻¹)	<i>t</i> -plot Micropore Volume (cm ³ g ⁻¹)	Cell parameter <i>a</i> (nm) XRD	Inner radius (nm) (SAXS)	Wall thickness (nm) SAXS
Me-IMO	615	0.35	0.085	3.02	0.91 (0.92 ^a)	0.55

^a Value for Me-IMO NTs re-suspended in water.

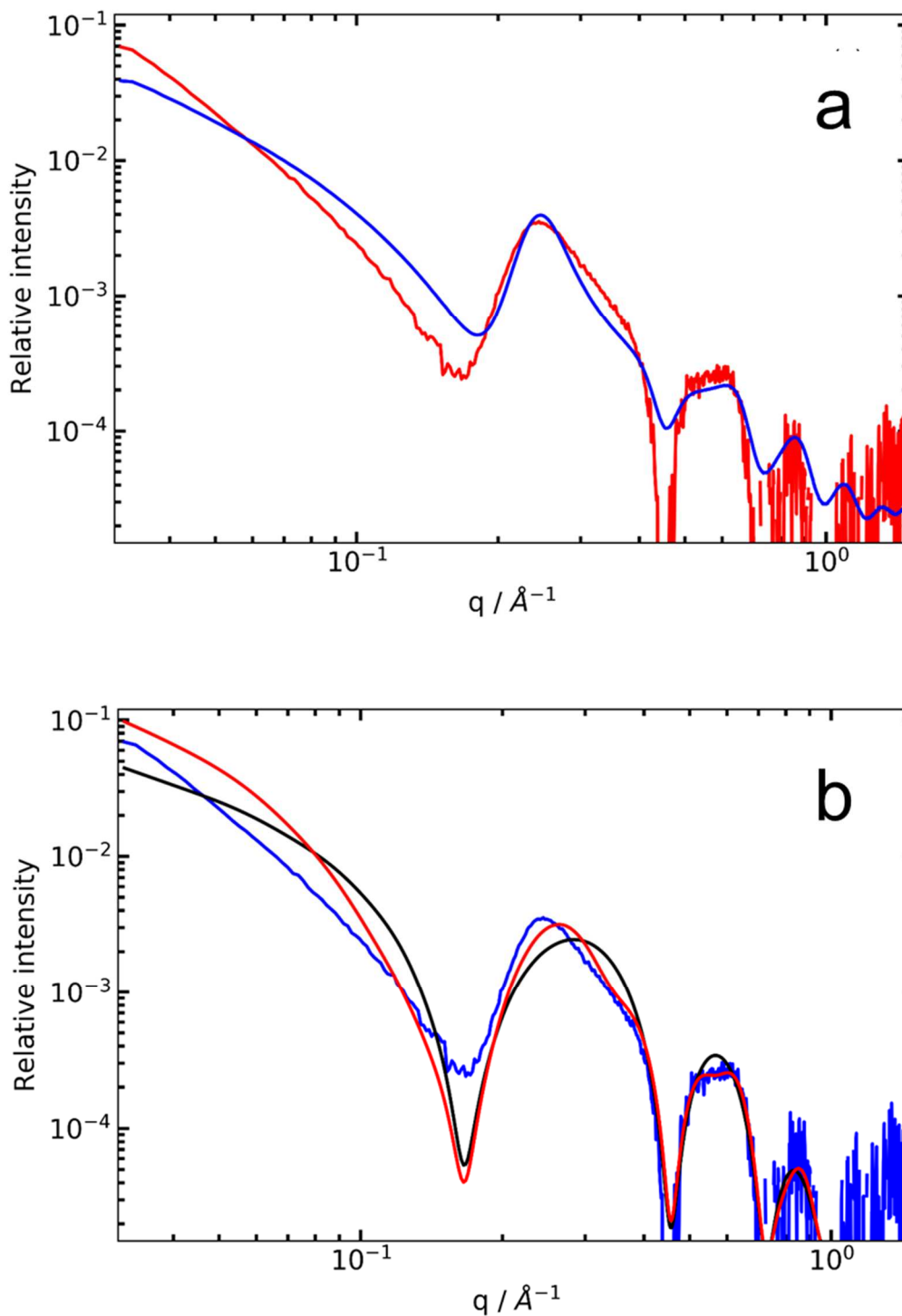
297

298 Figure 2a compares the SAXS spectra of the Me-IMO NTs powder under vacuum and of the
299 same re-dispersed in water (NTs concentration = 5 g L⁻¹): the two patterns are very close, indicating
300 that re-dispersion in water does not induce significant changes in the NTs shape. Only small
301 variations at small angles indicate that the NTs bundling may be slightly affected by re-dispersion
302 in water, with a consequent decrease of the average bundle size. The internal contrast is also
303 modified.

304 Fig. 2b compares the experimental SAXS pattern of Me-IMO NTs powder dispersed in
305 water (NTs concentration = 5 g L⁻¹) with the calculated patterns for isolated NTs and for NTs in
306 small bundles. In agreement with the powder XRD pattern, comparison of the SAXS curves clearly
307 indicates the presence of bundles when the powder is re-dispersed in water. The NTs inner radius,
308 as obtained by SAXS, is $r_i = 0.91$ nm and the wall thickness is $t_w = 0.55$ nm. The experimental peak
309 position in SAXS at $q = 0.238$ Å⁻¹ cannot be directly associated to the hexagonal lattice parameter
310 due to the peak shift induced by the NTs form factor. The lattice parameter that is obtained by the
311 computed SAXS pattern is 3.05 nm, i.e. a value that well corresponds to the NTs external diameter,
312 with a small additional separation of 0.15 nm.

313 The geometric values obtained from XRD and SAXS are in very good agreement with the
314 pores diameter as measured by N₂ isotherm. Indeed, according to the determined sizes, the
315 micropore volume is 0.095 cm³ g⁻¹, in fair agreement with the value as determined by the *t*-plot
316 method (0.085 cm³ g⁻¹). The small difference may be due to tiny amounts of water or anions trapped
317 within the B pores, which occupy a small part of the volume, finally explaining the 0.15 nm
318 additional distance in the bundle lattice parameter.

319



320

321

322

323

324

325

Figure 2. Section a: SAXS patterns of Me-IMO NTs as dry powder (blue curve) and re-
dispersed in water (5 g L⁻¹, red curve). Section b: SAXS pattern of NTs in water (blue curve)
compared to a scattering model of dispersed hollow NTs (with $r_i = 0.91$ nm, wall thickness = 0.55
nm, internal electronic density = $0.05 \text{ e}^-/\text{\AA}^3$, black curve) and to a scattering model considering
bundles (red curve).

326

327 The SAXS analysis also allowed obtaining the inner and outer electron density (ρ_i and ρ_e) of
328 the NTs in both the dry powder and after re-dispersion in water. Interestingly, ρ_i is equal to 0.05 e^-
329 $/\text{\AA}^3$ in both samples. As compared to the electron density of bulk water ($\rho_{\text{H}_2\text{O}} = 0.334 \text{ e}^-/\text{\AA}^3$), such a
330 low inner density means that in the powder (which was treated under vacuum at r.t. and not
331 outgassed at high temperature) only few H_2O molecules occur within the NTs and that the powder
332 is extremely hydrophobic, as ρ_i did not increase upon contact with water.

333

334 3.2. Adsorption of MCPA as studied in batch conditions and by SAXS

335 Fig. 3a shows the adsorbed amount of MCPA ($\mu\text{mol kg}^{-1}$) as a function of pH (each point
336 having being acquired after 24 h incubation): as a whole, the overall amount of adsorbed MPCA is
337 maximum below pH 4, decreasing as pH increases. Such a behaviour may be interpreted by
338 considering the ζ -potential curve in Fig. 1d, where the net positive charge of the NTs progressively
339 decreases as pH increases, until the PZC is reached (pH 8.6). In agreement with SAXS data in Fig.
340 5 (*vide infra*), the curve in Fig. 3a seems to point out the fact that the herbicide mainly interacts
341 with the NTs outer surface.

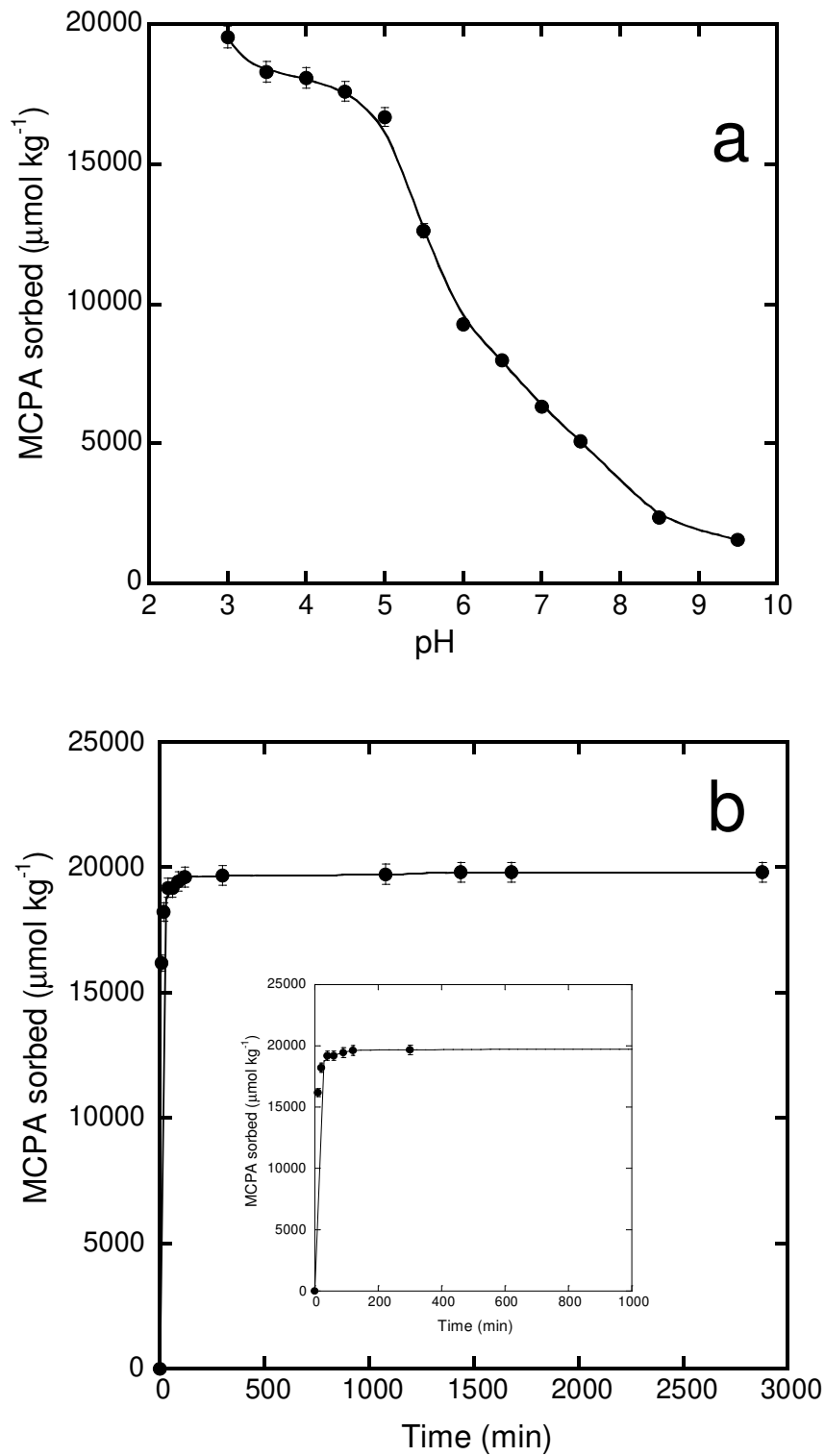
342 Fig. 3b shows the adsorbed amount of MCPA as a function of time at a constant pH of 3.5,
343 i.e. a pH value at which simultaneously the adsorbed amount is very high (Fig. 3a) and the NTs ζ
344 potential is ca. + 37 mV, a condition proper of a stable suspension (Honary and Zahir, 2013). In such
345 condition, aggregation of NTs into bundles should be limited, finally maximizing the available
346 external surface and, thus, MCPA adsorption. The curve in Fig. 3b shows indeed a steep increase in
347 the adsorbed MCPA during the first minutes (inset), reaching complete adsorption after 1440 min.
348 In the adopted experimental conditions (i.e. pH = 3.5 and initial concentration of MCPA = $1.0 \cdot 10^{-5}$
349 M), such a phenomenon can be readily assigned to the occurrence of electrostatic interactions. The

350 best model describing the sorption kinetics in Fig. 3b was the pseudo second-order model, which
351 can be expressed in a linear form according to eq. (2) (Ozacar and Sengyl, 2006):

352
$$\frac{t}{q} = \frac{1}{k_2 * q_e^2} - \frac{t}{q_e} \quad (2)$$

353 where q_e and q are the amount of organic pollutant adsorbed ($\mu\text{mol kg}^{-1}$ MCPA) at equilibrium and
354 at time t , respectively, k_2 is the rate constant of adsorption ($\text{kg}/\mu\text{mol h}$) and t is the time (h). For
355 MCPA, the following values were calculated $q_e = 19821.99 \mu\text{mol kg}^{-1}$ and $k_2 = 1.558 \times 10^{-3}$
356 $\text{kg}/\mu\text{mol h}$, with an $r^2 = 1$ confirming that the curve-fit procedure was appropriate.

357



358

359 **Figure 3.** Section a: MCPA adsorbed amount as a function of pH (incubation time = 24 h;

360 initial MCPA concentration = $1.0 \cdot 10^{-5}$ M). Section b: MCPA adsorbed amount as a function of time

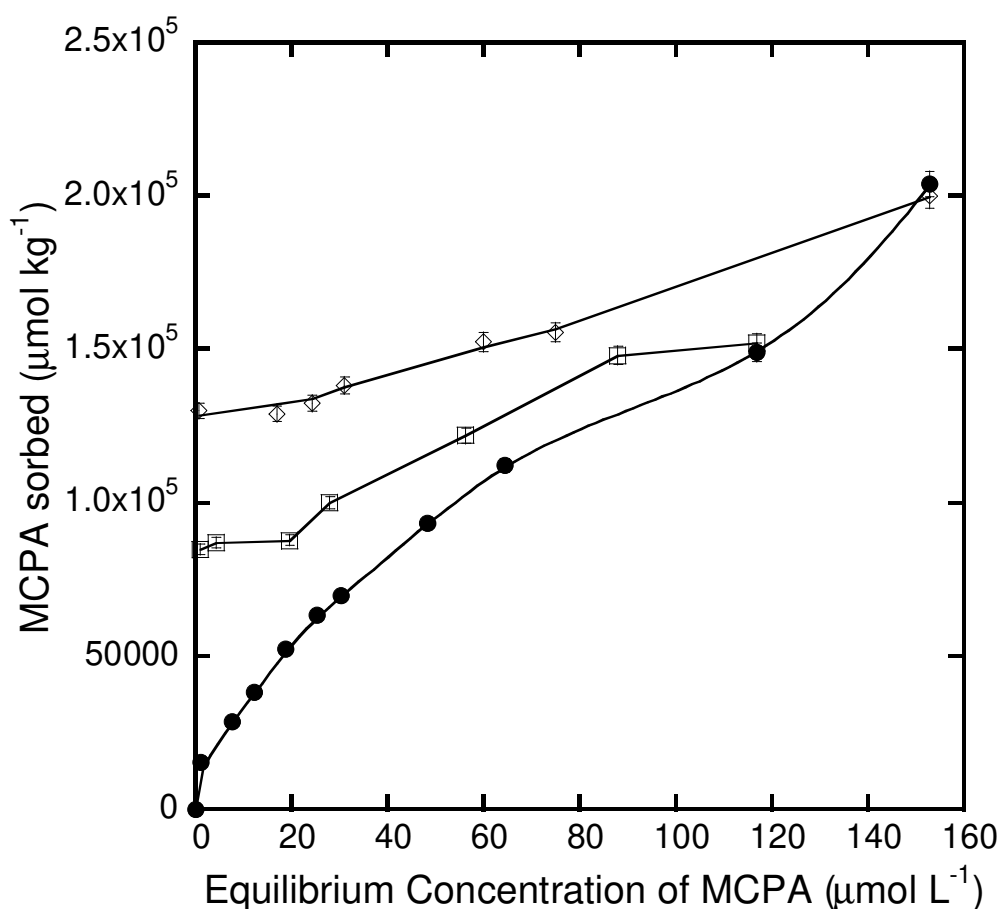
361 at pH = 3.5 (initial MCPA concentration = $1.0 \cdot 10^{-5}$ M). Inset to section b: magnification of the 0-
362 1000 min range.

363 Figure 4 reports MCPA adsorption/desorption equilibrium isotherms at pH = 3.5. The
364 adsorption isotherm (black symbols) has a complex shape, which can be due to multiple phenomena
365 occurring at the NTs outer surface at increasing MCPA concentration. Being the pKa of MCPA in
366 water equal to 2.90 (Addorisio et al., 2010), at pH = 3.5 its dissociation degree (α) is ca. 0.5 and,
367 thus, besides electrostatic interaction, other types of interactions may occur with the outer surface of
368 NTs, like H-bonding, as previously shown by some of us for MCPA adsorption on (mesoporous)
369 Al_2O_3 and Fe_2O_3 . (Addorisio et al., 2010) Interestingly, at higher MCPA equilibrium concentration,
370 the adsorption isotherm becomes convex, indicating that the adsorbing species has a lower affinity
371 for the adsorbent: multi-layer adsorption could, indeed, occur, as in MCPA crystals, where multiple
372 inter-molecular bonds form (Kobyłeczka et al., 2015).

373 So far, different adsorbents have been investigated for the removal of phenoxy herbicides,
374 including layered double hydroxides (Bruna et al., 2009; Ahmad et al., 2010; Kamaraj et al., 2014),
375 mesoporous metal oxides (Addorisio et al., 2010), resins (Ding et al., 2012) and carbon materials
376 (Kim et al., 2008). In particular, MCPA adsorption was studied on an Argentine montmorillonite
377 (MMT) and its organo-hybrid (OMMT) (Santiago et al., 2016): although adsorption on OMMT
378 (0.05 mol/kg) increased with respect to MMT (ca. 0.01 mol/kg), the MCPA adsorbed amounts were
379 significantly lower with respect to that obtained in the adopted experimental conditions with Me-
380 IMO NTs, i.e. ca. 0.2 mol/kg. Such a value is particularly sound if compared to the amount of
381 MCPA adsorbed at pH = 4.0 on a mesoporous alumina with $\text{SSA} = 195 \text{ m}^2 \text{ g}^{-1}$ (0.01 mol/kg), i.e. an
382 adsorbent with similar chemical composition, where diffusion limits occurred (Addorisio et al.,
383 2010).

384 Here, MCPA adsorption likely occurs at the outer surface of the NTs, thus overcoming the
385 aforementioned diffusion limitations during adsorption. However, the two desorption curves (white
386 symbols, Fig. 4) showed that, in the adopted experimental conditions, MCPA adsorption is only

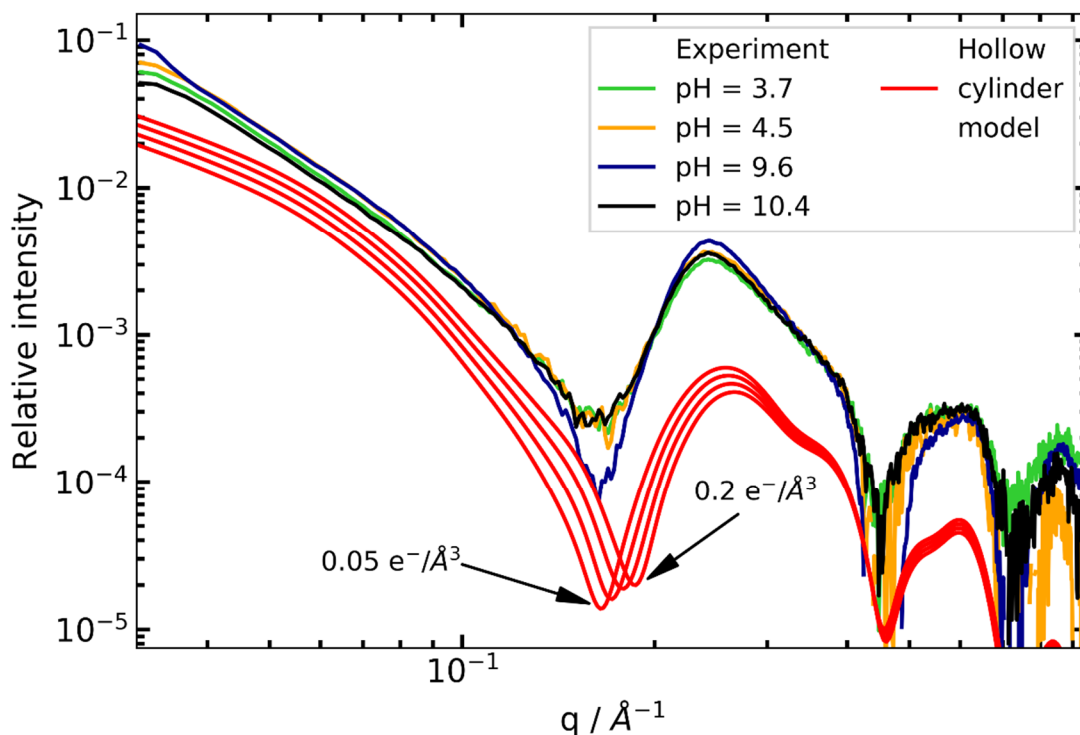
387 partially irreversible, in that the desorbed amount of MCPA was ca. the 35 % and the 44% of the
 388 total amount of adsorbed MCPA (when starting from 129820 $\mu\text{mol/kg}$ and 84790 $\mu\text{mol/kg}$.
 389 respectively). It should be noticed that MCPA adsorption at the outer surface of the NTs is surely
 390 perturbing their actual surface charge, which very likely decreases and, thus, the dispersion could
 391 become less stable, with consequent NTs agglomeration, finally hampering effective desorption of
 392 MCPA.



393
 394 **Figure 4.** Adsorption (black circles) isotherm and desorption (white symbols) isotherms of MCPA
 395 on Me-IMO-NTs as obtained at pH = 3.5 in the 0 -160 $\mu\text{mol L}^{-1}$ equilibrium concentration range.

396
 397 In order to confirm the preferential interaction with the outer surface of NTs, Figure 5a
 398 reports the SAXS spectra taken after contacting the Me-IMO NTs with MCPA $1.0 \cdot 10^{-4}$ M in water

399 at pH 3.7, 4.5, 9.6 and 10.4. The bulk electron density of MCPA is $\rho_{\text{MCPA}} = 0.48 \text{ e}^-/\text{\AA}^3$. In principle,
 400 the molecular size of MCPA (Table 1) allows adsorption within A pores: if so, a corresponding
 401 increase of the NTs inner electronic density should be measured by SAXS (Fig. 5), since the
 402 position of the first minimum of the scattered intensity is very sensitive to changes of the internal
 403 scattering length density. In order to better illustrate this, the scattered intensities of model NTs with
 404 internal electronic density varying from 0.05 to 0.2 $\text{e}^-/\text{\AA}^3$ are plotted in Fig. 5. Interestingly, the
 405 position of the first minimum of the experimental scattered intensity does not shift with pH. Such a
 406 constant inner NTs electronic density allows excluding any interaction of MCPA with the NTs inner
 407 surface.



408
 409 **Figure 5.** Experimental SAXS patterns of Me-IMO NTs in MCPA water suspensions at pH
 410 = 3.7, 4.5, 9.6 and 10.4 and calculated SAXS patterns (red curves), showing a shift of the scattering
 411 model of hollow cylinder at increasing internal electronic density (from 0.05 to 0.2 $\text{e}^-/\text{\AA}^3$).

412
 413 *3.3. Adsorption of DCM as studied in batch conditions and by SAXS.*

414 Figure 6a reports the pH dependence of DCM adsorbed on Me-IMO NTs: the curve shape is
415 very different with respect to that concerning MCPA (Fig. 3a), where the adsorbed amount
416 decreases with pH because, simultaneously, the NTs outer surface becomes less positively charged.
417 With DCM, adsorption is maximum at pH = 5.5 and, then, decreases.

418 DCM has a non-negligible dipole moment ($\mu = 1.470$ D) and can be polarized by the polar
419 outer NTs walls, leading to dipolar interactions. Simultaneously, its kinetic diameter (0.33 nm)
420 allows DCM diffusion within A pores, but also within B pores having a diameter of 0.45 nm,
421 (Bottero et al., 2011; Bonelli et al., 2013b) and which are able to strongly polarize $\text{CO}_{2(g)}$ molecules
422 in gas-solid systems (Zanzottera et al., 2012a; Bonelli et al., 2013b). Although different phenomena
423 affect adsorption in liquid/solid systems, it is interesting to notice that DCM adsorption is maximum
424 at pH 5.5, at which the ζ -potential of the Me-IMO NTs is ca. + 30 mV, likely implying some NTs
425 agglomeration with formation of (more) B pores, where the DCM molecules may diffuse and be
426 polarized, like $\text{CO}_{2(g)}$ molecules (Zanzottera et al., 2012a). Accordingly, the kinetic curve in Fig. 6b
427 has a smooth knee (inset) before reaching a plateau, indicating that more than one type of
428 interaction likely occurs. Application of eq. (2) to model the DCM sorption kinetics in Fig. 6b
429 (Ozacar and Sengyl, 2006) allowed calculating the following parameters: $q_e = 209.04$ mol kg^{-1} and
430 $k_2 = 0.0305$ kg/mol h, $r^2 = 0.99$. The extremely high amount of adsorbed DCM could be explained
431 by considering that in oil/water emulsions, such hybrid NTs adsorb at the oil/water interface,
432 stabilizing Pickering emulsions (Picot et al., 2016), modifying the viscosity and, possibly, favouring
433 transport of small molecules within the NTs.

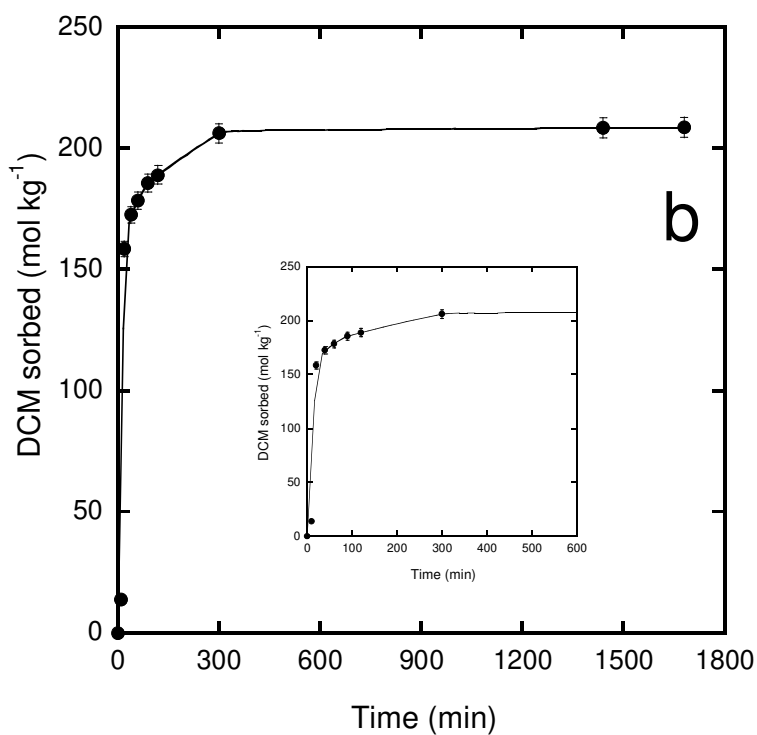
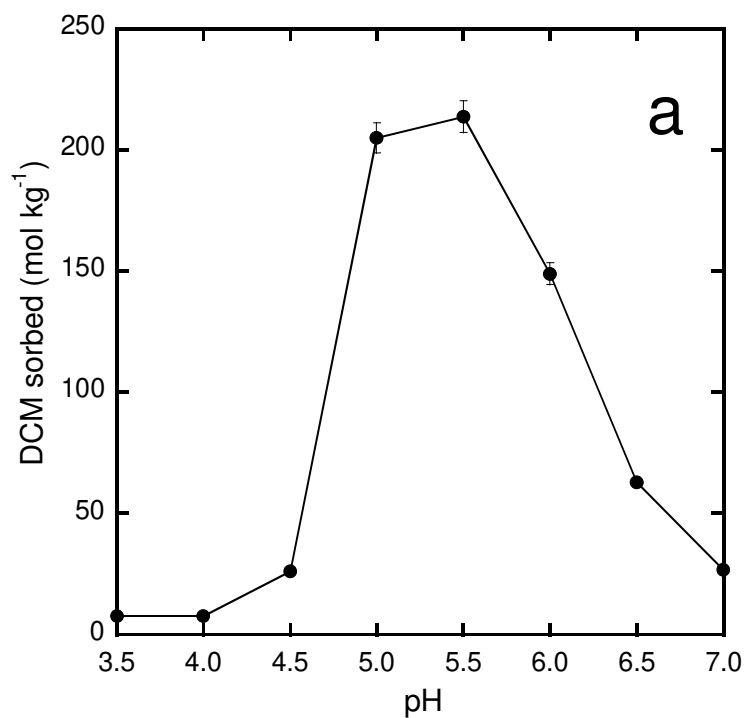
434 Accordingly, the adsorption isotherm in Fig. 7 (black symbols) has an S-shape, indicating
435 that at least two types of adsorption phenomena occur: at low concentration, DCM molecules
436 should interact with stronger adsorbing sites, since their sizeable dipole moment allows interaction
437 with polarizing sites, like B pores, stemming from partial NTs agglomeration into small bundles,
438 and able to polarize DCM molecules (kinetic diameter = 0.33 nm). At increasing pH value, the
439 outer surface of NTs (C surface) becomes less positively charged, thus lowering the adsorption

440 capacity of the outer surface of the NTs towards DCM molecules. Unfortunately, the electronic
441 density of DCM (Table 1) is very close to that of water ($\rho_{\text{H}_2\text{O}} = 0.334 \text{ e}^-/\text{\AA}^3$) and, thus, if such a
442 phenomenon should happen, it would be hardly discernible by SAXS, which instead could readily
443 show DCM diffusion within the NTs (A pores, *vide infra*). The latter phenomenon is likely
444 responsible of the largest adsorbed amount of DCM above 0.02 mol/L equilibrium concentration,
445 although in those conditions an oil-in-water Pickering emulsion could form (Picot et al., 2016).

446 As a whole, the thorough understanding of the interaction of DCM with Me-IMO NTs is
447 complicated both by the nature of the pollutant and by formation of Pickering emulsions (Picot et
448 al., 2016).

449 Concerning DCM removal from polluted water, adsorption is considered by the literature as
450 one the most applicable techniques (Lemus et al., 2012; Zhou et al., 2014, 2017), but it requires
451 porous materials with sound adsorbing capacity and high stability. The DCM adsorption capacity of
452 Zr-based metal-organic framework (UiO-66) was enhanced in the presence of UiO-66 crystals with
453 various morphologies and optimized porous structure as obtained by adjusting the synthesis
454 procedure.(Zhou et al., 2017): however, in the adopted experimental conditions, the maximum
455 adsorption capacity was lower than here (ca. 6 mmol/kg).

456 As for MCPA, in the adopted experimental conditions DCM desorption was not fully
457 reversible (white symbols in Fig. 7) indicating the likely occurrence of mass transfer phenomena,
458 related to some NTs aggregation, which hampers DCM molecules diffusion of DCM from the
459 interior of the NTs/bundles to the exterior. However, such diffusion limitations, occurring
460 especially during desorption, could be overcome by changing operative conditions, e.g. liquid/solid
461 ratio, and require dedicated studies.



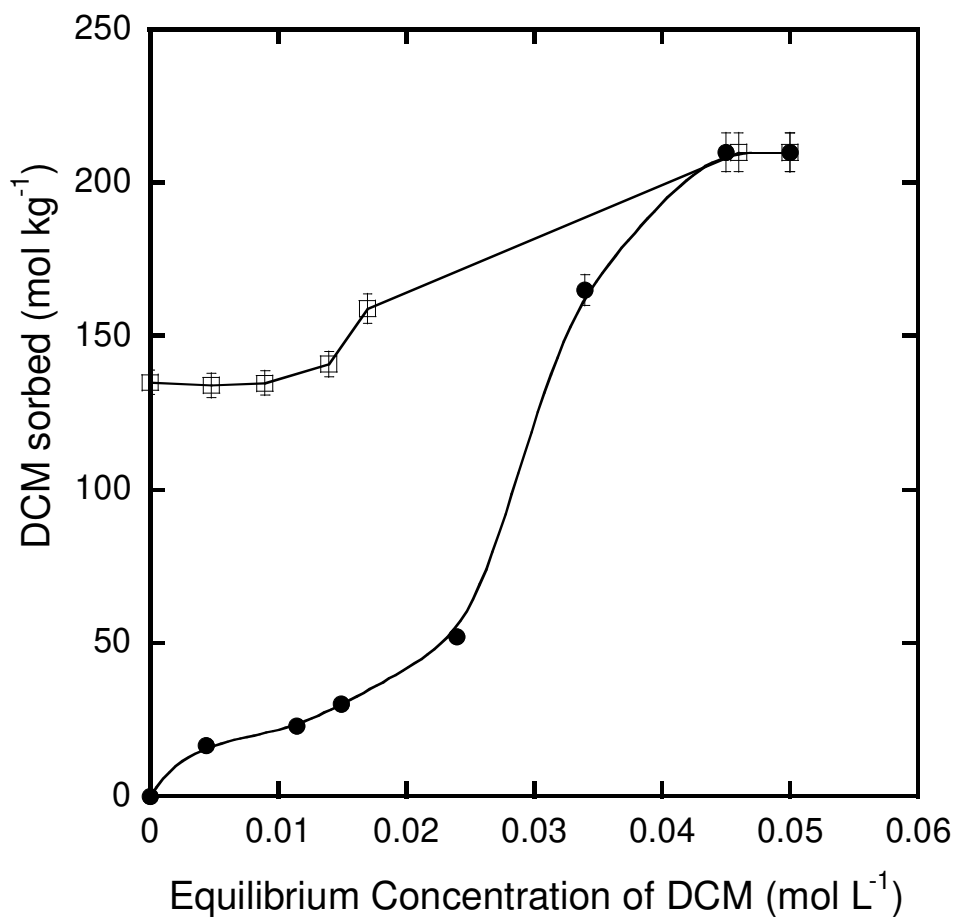
462

463

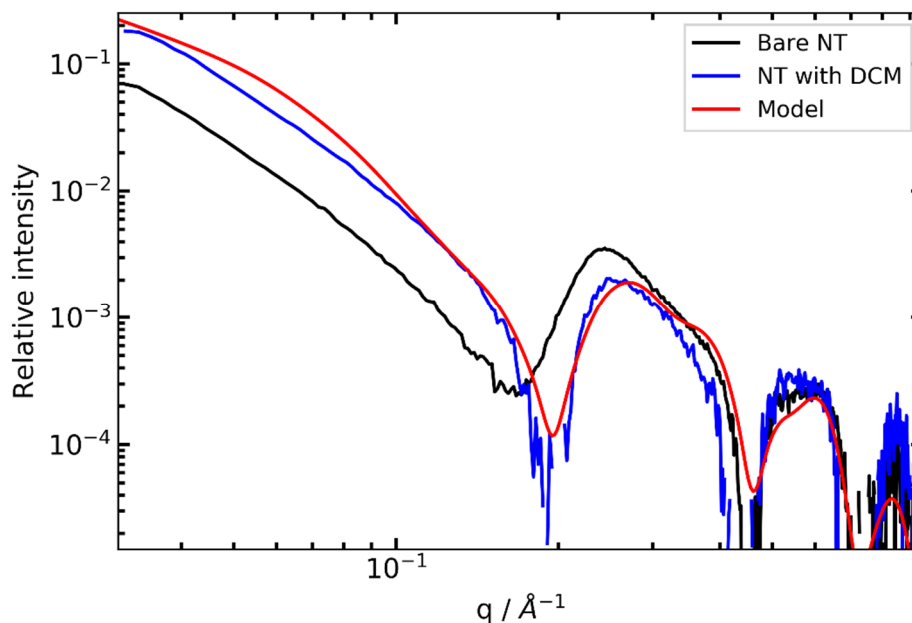
464 **Figure 6.** Section a: DCM adsorbed amount as a function of pH. Incubation time: 24 h.

465 Initial DCM concentration: 0.15 M. Section b: DCM adsorbed amount as a function of time. pH =

466 5.5; initial DCM concentration: 0.15 M. Inset to section b: magnification of the 0-600 min range,
467 where the maximum amount of adsorbed DCM is reached after 300 min.
468



469
470
471 **Figure 7.** Adsorption (black symbols) isotherm and desorption isotherm (white symbols) of DCM
472 on Me-IMO-NTs at pH = 5.5 in the 0 -0.06 mol L⁻¹ equilibrium concentration range.
473



474

475 **Figure 8.** SAXS patterns of Me-IMO NTs in the DCM suspension at natural pH. The scattering
 476 model for a hollow cylinder show the variation of internal electronic density from 0.05 to 0.29 e^-
 477 $/\text{\AA}^3$.

478

479 Fig. 8 reports the SAXS patterns observed when the NTs are contacted with DCM
 480 suspension. The position of the first minimum shifts towards higher q values, indicating an increase
 481 of the inner electronic density. The applied model yields a value of ρ_i equal to 0.29 $e/\text{\AA}^3$ for the
 482 inner electron density of Me-IMO NTs, proving that DCM (bulk DCM has $\rho = 0.4 e/\text{\AA}^3$, Table 1)
 483 has indeed entered the NTs. The high adsorbed amounts measured by batch experiments indicate
 484 that the DCM molecules adsorb also at the outer surface of NTs and not only within them, but since
 485 the SAXS measurement is based on a change on the internal electron density, it may be unable to
 486 detected the change in the outer electron density, since the NTs are suspended in water, which has a
 487 high electron density.

488

489 **Conclusions**

490 Methylmogolite NTs have two types of surface, namely an inner one, which is extremely
491 hydrophobic, and an outer one, which is hydrophilic, polar and positively charged below pH 8.6.
492 The external positive charge affects the NTs behaviour in water: for instance, by varying pH, NTs
493 arrangement changes, likely leading to some aggregation phenomena that, in turn, affect both
494 adsorption and desorption processes in water.

495 Adsorption of two organic pollutants (namely MCPA, 2-methyl-4-chlorophenoxyacetic acid,
496 and DCM, dichloromethane) on methylmogolite occurs through complex interactions, which can
497 be only partially explained by the joint use of batch experiments and SAXS measurements.

498 On the one hand, the reported results show that MCPA adsorption occurs at the outer surface
499 of the NTs by means of both electrostatic interactions and intermolecular forces, with sound overall
500 adsorbed amounts as compared to another mesoporous adsorbent (i.e. Al_2O_3) with a chemical
501 composition similar to that of the NTs outer surface.

502 On the other hand, unravelling the type of interaction of DCM with methylmogolite is not
503 straightforward. SAXS measurements clearly showed diffusion of DCM molecules within A pores
504 and batch experiments showed high adsorbed amounts. However, the latter type of measurements
505 seem to point out the interaction with another type of surface, most likely B pores forming among
506 three aligned NTs in a bundle: unfortunately, this type of interaction that cannot be clearly assessed
507 by SAXS. Moreover, on the basis of previous studies, stabilization of an emulsion induced by the
508 same NTs could not be excluded.

509 To the best of our knowledge, this is the first work assessing the adsorption/desorption of
510 organic molecules of environmental concern with this type of nanomaterial and could open new
511 perspectives for its practical application, undoubtedly after optimization of the desorption process,
512 which requires dedicated studies.

513

514 **Acknowledgements**

515 Financial support from Università Italo-Francese (Galileo Project Grant n°G16 – 34 «Hybrid
516 imogolite nanotubes for environmental applications») is acknowledged.

517

518 **References**

519 Ackerman, W.C., Smith, D.M., Huling, J.C., Kim, Y.W., Bailey, J.K., Brinker, C.J., 1993.

520 Gas/Vapor Adsorption in Imogolite: A Microporous Tubular Aluminosilicate. *Langmuir* 9,
521 1051–1057. <https://doi.org/10.1021/la00028a029>

522 Addorisio, V., Esposito, S., Sannino, F., 2010. Sorption Capacity of Mesoporous Metal Oxides for
523 the Removal of MCPA from Polluted Waters. *J. Agric. Food Chem.* 58, 5011–5016.

524 <https://doi.org/10.1021/jf9044815>

525 Ahmad, T., Rafatullah, M., Ghazali, A., Sulaiman, O., Hashim, R., Ahmad, A., 2010. Removal of
526 pesticides from water and wastewater by different adsorbents: A review. *J. Environ. Sci. Heal.*
527 - Part C Environ. Carcinog. Ecotoxicol. Rev. 28, 231–271.

528 <https://doi.org/10.1080/10590501.2010.525782>

529 Amara, M.S., Paineau, E., Tache, O., Launois, P., Thill, A., 2015. Hybrid , Tunable-Diameter ,
530 Metal Oxide Nanotubes for Trapping of Organic Molecules.

531 <https://doi.org/10.1021/cm503428q>

532 Bahadori, E., Vaiano, V., Esposito, S., Armandi, M., Sannino, D., Bonelli, B., 2018. Photo-
533 activated degradation of tartrazine by H₂O₂ as catalyzed by both bare and Fe-doped methyl-
534 imogolite nanotubes. *Catal. Today* 304, 199–207. <https://doi.org/10.1016/j.cattod.2017.08.003>

535 Bonelli, B., 2016. Surface Chemical Modifications of Imogolite, in: Yuan, P., Thill, A., Bergaya, F.
536 (Eds.), *Developments in Clay Science*. Elsevier B.V, pp. 279–307.

537 <https://doi.org/10.1016/B978-0-08-100293-3.00012-1>

- 538 Bonelli, B., Armandi, M., Garrone, E., 2013a. Surface properties of alumino-silicate single-walled
539 nanotubes of the imogolite type. *Phys. Chem. Chem. Phys.* 15, 13381–13390.
540 <https://doi.org/10.1039/c3cp51508g>
- 541 Bonelli, B., Bottero, I., Ballarini, N., Passeri, S., Cavani, F., Garrone, E., 2009. IR spectroscopic
542 and catalytic characterization of the acidity of imogolite-based systems. *J. Catal.* 264, 15–30.
543 <https://doi.org/10.1016/j.jcat.2009.03.003>
- 544 Bonelli, B., Zanzottera, C., Armandi, M., Esposito, S., Garrone, E., 2013b. IR spectroscopic study
545 of the acidic properties of alumino-silicate single-walled nanotubes of the imogolite type.
546 *Catal. Today* 218–219, 3–9. <https://doi.org/10.1016/j.cattod.2013.02.004>
- 547 Bottero, I., Bonelli, B., Ashbrook, S.E., Wright, P.A., Zhou, W., Tagliabue, M., Armandi, M.,
548 Garrone, E., 2011. Synthesis and characterization of hybrid organic/inorganic nanotubes of the
549 imogolite type and their behaviour towards methane adsorption. *Phys. Chem. Chem. Phys.* 13,
550 744–750. <https://doi.org/10.1039/c0cp00438c>
- 551 Boyer, M., Paineau, E., Bacia-verloop, M., Thill, A., 2014. Applied Clay Science Aqueous
552 dispersion state of amphiphilic hybrid aluminosilicate nanotubes. *Appl. Clay Sci.* 96, 45–49.
553 <https://doi.org/10.1016/j.clay.2014.04.022>
- 554 Bruna, F., Celis, R., Pavlovic, I., Barriga, C., Cornejo, J., Ulibarri, M.A., 2009. Layered double
555 hydroxides as adsorbents and carriers of the herbicide (4-chloro-2-methylphenoxy)acetic acid
556 (MCPA): Systems Mg-Al, Mg-Fe and Mg-Al-Fe. *J. Hazard. Mater.* 168, 1476–1481.
557 <https://doi.org/10.1016/j.jhazmat.2009.03.038>
- 558 Bursill, L.A., Peng, J.L., Bourgeois, L.N., 2000. Imogolite : An aluminosilicate nanotube material.
559 *Philos. Mag. A* 80, 105–117. <https://doi.org/10.1080/01418610008212043>
- 560 Cradwick, P.D.G., Farmer, V.C., Russell, J.D., Masson, C.R., Wada, K., Yoshinaga, N., 1972.

561 Imogolite, a Hydrated Aluminium Silicate of Tubular Structure. *Nat. Phys. Sci.* 240, 187–189.
562 <https://doi.org/10.1038/physci240187a0>

563 Ding, L., Lu, X., Deng, H., Zhang, X., 2012. Adsorptive removal of 2,4-dichlorophenoxyacetic acid
564 (2,4-D) from aqueous solutions using MIEX resin. *Ind. Eng. Chem. Res.* 51, 11226–11235.
565 <https://doi.org/10.1021/ie300469h>

566 Du, P., Yuan, P., Thill, A., Annabi-Bergaya, F., Liu, D., Wang, S., 2017. Insights into the formation
567 mechanism of imogolite from a full-range observation of its sol-gel growth. *Appl. Clay Sci.*
568 150, 115–124. <https://doi.org/10.1016/j.clay.2017.09.021>

569 Freyria, F.S., Geobaldo, F., Bonelli, B., 2018. Nanomaterials for the abatement of pharmaceuticals
570 and personal care products from wastewater. *Appl. Sci.* 8, 170.
571 <https://doi.org/10.3390/app8020170>

572 Garrone, E., Bonelli, B., 2016. Imogolite for Catalysis and Adsorption, in: Yuan, P., Thill, A.,
573 Bergaya, F. (Eds.), *Developments in Clay Science*. Elsevier B.V, pp. 672–707.
574 <https://doi.org/10.1016/B978-0-08-100293-3.00025-X>

575 Gimeno, O., Plucinski, P., Kolaczowski, S.T., Rivas, F.J., Alvarez, P.M., 2003. Removal of the
576 Herbicide MCPA by Commercial Activated Carbons : Equilibrium , Kinetics , and
577 Reversibility 22, 1076–1086. <https://doi.org/10.1021/ie020424x>

578 Gustafsson, J.P., 2001. The surface chemistry of imogolite. *Clays Clay Miner.* 49, 73–80.

579 Honary, S., Zahir, F., 2013. Effect of Zeta Potential on the Properties of Nano-Drug Delivery
580 Systems - A Review (Part 2) 12, 265–273.

581 Huang, B., Lei, C., Wei, C., Zeng, G., 2014. Chlorinated volatile organic compounds (Cl-VOCs)
582 in environment — sources , potential human health impacts , and current remediation
583 technologies. *Environ. Int.* 71, 118–138. <https://doi.org/10.1016/j.envint.2014.06.013>

584 Kamaraj, R., Davidson, D.J., Sozhan, G., Vasudevan, S., 2014. An in situ electrosynthesis of metal
585 hydroxides and their application for adsorption of 4-chloro-2-methylphenoxyacetic acid
586 (MCPA) from aqueous solution. *J. Environ. Chem. Eng.* 2, 2068–2077.
587 <https://doi.org/10.1016/j.jece.2014.08.027>

588 Karube, J., 1998. Notes: Hysteris of the colloidal stability of imogolite. *Clays Clay Miner.* 583–584.
589 <https://doi.org/10.1346/CCMN.1998.0460512>

590 Kim, T.Y., Park, S.S., Kim, S.J., Cho, S.Y., 2008. Separation characteristics of some phenoxy
591 herbicides from aqueous solution. *Adsorption* 14, 611–619. [https://doi.org/10.1007/s10450-](https://doi.org/10.1007/s10450-008-9129-6)
592 [008-9129-6](https://doi.org/10.1007/s10450-008-9129-6)

593 Kobylecka, J., Turek, A., Siero, L., 2015. Crystal Packing and Supramolecular Motifs in Four
594 Phenoxyalkanoic Acid Crystal Packing and Supramolecular Motifs in Four Phenoxyalkanoic
595 Acid Herbicides — Low-Temperature Redeterminations. *Org. Chem. Int.* ID 608165.
596 <https://doi.org/10.1155/2011/608165>

597 Lemus, J., Martin-Martinez, M., Palomar, J., Gomez-Sainero, L., Gilarranz, M.A., Rodriguez, J.J.,
598 2012. Removal of chlorinated organic volatile compounds by gas phase adsorption with
599 activated carbon. *Chem. Eng. J.* 211–212, 246–254. <https://doi.org/10.1016/j.cej.2012.09.021>

600 Mackenzie, K.J.D., 1989. Structure and Thermal Transformations of Imogolite Studied by ²⁹Si and
601 ²⁷Al High-Resolution Solid-State Nuclear Magnetic Resonance. *Clays Clay Miner.* 37, 317–
602 324. <https://doi.org/10.1346/CCMN.1989.0370404>

603 Mizota, C., 1977. Phosphate fixation by ando soils different in their clay mineral composition. *Soil*
604 *Sci. Plant Nutr.* 23, 311–318. <https://doi.org/10.1080/00380768.1977.10433050>

605 Ozacar, M., Sengyl, I., 2006. A two stage batch adsorber design for methylene blue removal to
606 minimize contact time. *J. Environ. Manag.* 80, 372–379.

607 <https://doi.org/10.1016/j.jenvman.2005.10.004>

608 Parfitt, R.L., 2009. Allophane and imogolite : role in soil biogeochemical processes. *Clay Miner.*
609 44, 135–155. <https://doi.org/10.1180/claymin.2009.044.1.135>

610 Picot, P., Gobeaux, F., Coradin, T., Thill, A., 2019. Dual internal functionalization of imogolite
611 nanotubes as evidenced by optical properties of Nile red. *Appl. Clay Sci.* 178, 1015133.
612 <https://doi.org/10.1016/j.clay.2019.105133>

613 Picot, P., Malloggi, F., Coradin, T., Thill, A., 2016. Behaviour of hybrid inside/out Janus nanotubes
614 at an oil/water interface. A route to self-assembled nanofluidics? *Faraday Discuss.* 191, 1–5.
615 <https://doi.org/10.1039/C6FD00034G>

616 Poli, E., Elliott, J.D., Hine, N.D.M., Mostofi, A.A., Teobaldi, G., Elliott, J.D., Hine, N.D.M.,
617 Mostofi, A.A., Teobaldi, G., Poli, E., Elliott, J.D., Hine, N.D.M., Mostofi, A.A., Teobaldi, G.,
618 2015. Large-scale density functional theory simulation of inorganic nanotubes : a case study on
619 Imogolite nanotubes 19, S272. <https://doi.org/10.1179/1432891715Z.0000000001560>

620 Rojas-Mancilla, E., Oyarce, A., Alvarado-soto, L., Ram, R., 2019. Imogolite Synthetized in
621 Presence of As(III) Induces Low Cell Toxicity and Hemolysis , in Vitro , Potential
622 Stabilization of Arsenite Present in Aqueous Systems 4, 10510–10515.
623 <https://doi.org/10.1021/acsomega.8b03357>

624 Santiago, C.C., Fernández, M.A., Torres Sánchez, R.M., 2016. Adsorption and characterization of
625 MCPA on DDTMA- and raw-montmorillonite: Surface sites involved. *J. Environ. Sci. Heal. -*
626 *Part B Pestic. Food Contam. Agric. Wastes* 51, 245–253.
627 <https://doi.org/10.1080/03601234.2015.1120618>

628 Shafia, E., Esposito, S., Armandi, M., Bahadori, E., Garrone, E., Bonelli, B., 2016a. Reactivity of
629 bare and Fe-doped alumino-silicate nanotubes (imogolite) with H₂O₂ and the azo-dye Acid

630 Orange 7. *Catal. Today* 277, 89–96. <https://doi.org/10.1016/j.cattod.2015.10.011>

631 Shafia, E., Esposito, S., Bahadori, E., Armandi, M., Manzoli, M., Bonelli, B., 2016b. Synthesis and
632 characterization of Fe-doped aluminosilicate nanotubes with enhanced electron conductive
633 properties. *J. Vis. Exp.* 117, e54758. <https://doi.org/10.3791/54758>

634 Thill, A., Picot, P., Belloni, L., 2017. A mechanism for the sphere/tube shape transition of
635 nanoparticles with an imogolite local structure (imogolite and allophane). *Appl. Clay Sci.* 141,
636 308–315. <https://doi.org/10.1016/j.clay.2017.03.011>

637 Zanzottera, C., Armandi, M., Esposito, S., Garrone, E., Bonelli, B., 2012a. CO₂ adsorption on
638 aluminosilicate single-walled nanotubes of imogolite type. *J. Phys. Chem. C* 116, 20417–
639 20425. <https://doi.org/10.1021/jp3061637>

640 Zanzottera, C., Vicente, A., Armandi, M., Fernandez, C., Garrone, E., Bonelli, B., 2012b. Thermal
641 collapse of single-walled alumino-silicate nanotubes: Transformation mechanisms and
642 morphology of the resulting lamellar phases. *J. Phys. Chem. C* 116, 23577–23584.
643 <https://doi.org/10.1021/jp3090638>

644 Zhou, L., Chen, Y.L., Zhang, X.H., Tian, F.M., Zu, Z.N., 2014. Zeolites developed from mixed
645 alkali modified coal fly ash for adsorption of volatile organic compounds. *Mater. Lett.* 119,
646 140–142. <https://doi.org/10.1016/j.matlet.2013.12.097>

647 Zhou, L., Zhang, X., Chen, Y., 2017. Modulated synthesis of zirconium metal–organic framework
648 UiO-66 with enhanced dichloromethane adsorption capacity. *Mater. Lett.* 197, 167–170.
649 <https://doi.org/10.1016/j.matlet.2017.03.162>

650

651

